

Full paper

Expanded lithiation of titanium disulfide: Reaction kinetics of multi-step conversion reaction



Maosen Fu^{a,b,1}, Zhenpeng Yao^{c,g,1}, Xiao Ma^a, Hui Dong^d, Ke Sun^e, Sooyeon Hwang^b, Enyuan Hu^f, Hong Gan^e, Yan Yao^d, Eric A. Stach^h, Chris Wolverton^c, Dong Su^{b,*}

^a Shanxi Materials Analysis and Research Center, School of Materials Science and Engineering, Northwestern Polytechnical University, Xi'an, 710000, PR China

^b Center for Functional Nanomaterials, Brookhaven National Laboratory, Upton, NY, 11973, United States

^c Department of Materials Science and Engineering, Northwestern University, 2220 Campus Drive, Evanston, IL, 60208, United States

^d Department of Electrical & Computer Engineering and TcSUH, University of Houston, Houston, TX, 77204, United States

^e Energy Sciences Directorate, Brookhaven National Laboratory, Upton, NY, 11973, United States

^f Chemistry Division, Brookhaven National Laboratory, Upton, NY, 11973, United States

^g Department of Chemistry and Chemical Biology, Harvard University, 12 Oxford Street, Cambridge, MA, 02138, USA

^h Department of Materials Science and Engineering, University of Pennsylvania, Philadelphia, PA, 19104, United States

ARTICLE INFO

Keywords:

Lithium ion battery
2D metal chalcogenides
Conversion reaction
In situ transmission electron microscopy
Lithiation

ABSTRACT

Phase evolution during a thorough Li ion's insertion of electrode materials governs their battery performance during charge and discharge. Here we investigated the lithiation pathway of titanium disulfide using *in situ* TEM combined with synchrotron-based pair distribution function measurement and first-principles calculations. A 2D intercalation reaction proceeds along with a transition from van der Waals interaction between Ti–S slabs to the covalent bonding of S–Li–S, with no symmetry broken. Further lithiation triggers unconventionally multiple step conversion reactions as proved: $\text{LiTiS}_2 \rightarrow \text{TiS} \rightarrow \text{Ti}_2\text{S} \rightarrow \text{Ti}$. The conversion reaction pathway is also verified in fully discharged sample in coin-cell. The expanded conversion chemistry is supposed to increase the capacity of TiS_2 electrode and downgrade the cyclability, whereas the existence of intermediate phases shows the promise of improving the reversibility with a successful control of the state of charge.

1. Introduction

Battery technologies with high energy density are greatly demanded for efficient usage of renewable energy and extending the driving range of electric vehicles (EVs). Searching for electrode materials capable of (de-)accommodating a larger amount of charged ions (e.g. Li^+ , Na^+), like transition metal (TM) oxides and sulfides, has drawn significant attention in the field of Li(Na)-ion battery [1]. The phase evolution of electrode material during a thorough ion accommodation (or extraction) governs the reversible charged ion uptake (removal). However, it is difficult to track experimentally because of the existence of possible mixed reactions as well as the transient metastable phases [2–4]. While synchrotron-based X-ray techniques play an essential role in determining the intermediate states at the micron-scale [5], recent advances in transmission electron microscopy (TEM) show great promises of visualizing the reaction dynamics of battery materials at atomic resolution [6–10]. Here, we explore the structural evolution in a 2-

dimensional (2D) metal chalcogenide compound, TiS_2 , during its lithiation, *via* a first-principles calculation guided *in situ* TEM approach.

2D metal chalcogenides have attracted intensive attentions for a variety of promising applications such as nanoelectronics, photonics, sensors and electrodes for energy storage systems [11–13]. Their distinct structural property, 2D hexagonal layers bonded by van der Waals force, makes them highly attractive for energy storage as alkaline ions can be intercalated into these adjacent metal-sulfur layers [14,15]. Among those 2D-layered chalcogenides, TiS_2 is a cheap, environmentally-friendly compound which was the first compound explored as a cathode pioneered by Whittingham et al. in 1970s [15,16]. Only intercalation process from TiS_2 to LiTiS_2 has been reported so far, $\text{TiS}_2 + x\text{Li}^+ + e^- \rightarrow \text{Li}_x\text{TiS}_2$, $0 \leq x \leq 1$, which provides a capacity of 239 mAh/g at a discharge potential of 1.8 V [14,17–18]. However, the full lithiation mechanism of TiS_2 was not fully understood. There are possible intermediate phases during the reaction. These issues will determine the discharge potential as well as the reaction kinetics. On

* Corresponding author.

E-mail address: dsu@bnl.gov (D. Su).

¹ equal contribution.

the other hand, the limited energy density is another problem for the application of TiS_2 as cathode. Further lithiation may provide extra capacity but have not been explored. Up to now, it is not clear whether LiTiS_2 is thermodynamically stable and there is possibly a conversion reaction with further lithiation.

In this work, we investigate the phase evolution of 1T-TiS_2 in the whole range of discharge using a multimodal approach including density functional theory calculations, electrochemical tests, synchrotron X-ray pair distribution function (PDF) analysis, and *in situ* TEM. Phase transformations during full lithiation of TiS_2 are predicted using the (non)equilibrium phase search with a consideration of mixed intercalation and conversion reaction processes as a function of Li composition. First-principles calculations demonstrate that TiS , Ti_2S , and Ti phases can be the thermodynamically stable at higher lithium concentrations (Li_xTiS_2 where $x > 1$). *In situ* electron diffraction and TEM imaging results confirm the multi-step conversion reactions and validated existences of these intermediate phases, after the initial intercalation reaction from TiS_2 to LiTiS_2 . The expanded lithiation may largely increase the energy density of TiS_2 . Precise corroboration of phase evolutions in TiS_2 in this work demonstrates the advantage of combining DFT calculations with *in situ* TEM for exploring the reaction mechanisms of electrodes for secondary ion batteries, and the important role of M-S bonds in determining the reaction pathway.

2. Materials and methods

2.1. Materials

Commercially available layered TiS_2 (99.8%, Strem Chemical Inc.) with an average particle size of $10\ \mu\text{m}$ was used for this work. The sample is nanoplate and the thickness of the nanoplates are about tens of nanometers.

2.2. Electrochemical measurements

The composite electrode was prepared as a mixed slurry of 80 wt% TiS_2 , 10 wt% carbon black and 10 wt% polyvinylidene fluoride (PVDF) binder in an N-methyl pyrrolidone (NMP) solvent. The slurry was casted on a Al foil current collector. 2032-type of coin cells were assembled inside an argon-filled glove box with the as-prepared TiS_2 electrode, Celgard separator, Li metal and an electrolyte of 1 M lithium hexafluorophosphate (LiPF_6) in ethylene carbonate (EC): dimethyl carbonate (DMC) (1:1 in weight). Battery test were performed on Arbin BT2000 battery test station with a current rate of 50 mA/g.

2.3. TEM characterization

For the post-mortem analysis, Cu TEM grids with TiS_2 sample were incorporated into coin cells with composite electrodes. After designated potential of 0.01 V (discharged) or 3 V (charged) had been reached, the coin cells were disassembled and TEM grids were cleaned with DMC solution inside an argon-filled glove box. Ex-situ and *in situ* TEM observations were performed with a JEM-2100F transmission electron microscope (JEOL) at an acceleration voltage of 200 kV. The *in situ* TEM cell was incorporated into a Nanofactory TEM-STM specimen holder, where TiS_2 dispersed on a TEM half-grid with lacey carbon support are analogous to active electrode material, current collector, and carbon binders, respectively; Li metal was coated on to a piezo-driven tungsten probe as the counter electrode, and a thin layer of Li_2O formed on Li metal as the solid electrolyte. A negative voltage of $-5\ \text{V} \sim -10\ \text{V}$ was applied between tip and sample to prompt the diffusion of lithium and trigger the lithiation process. The high-resolution STEM imaging and STEM-EELS were conducted on a Hitachi HD2700C STEM operated at 200 kV and equipped with a probe aberration corrector (spatial resolution $< 1\ \text{\AA}$ and energy resolution $\sim 0.35\ \text{eV}$).

In case of high-resolution imaging, a high dose of electron beam

may bring artifacts and induce decomposition of metal compounds, which should always be avoided [19,20]. In order to minimize radiation effect, we controlled both electron dose rate (beam intensity) and total dose (exposure time) as low as possible during observation. In addition, a controlled *in situ* HRTEM experiment was conducted with at similar imaging conditions in order to clarify the electron beam irradiation effects on the *in situ* HRTEM results.

2.4. PDF characterization

Pair distribution function experiments were carried out at XPD beamline (X-ray Powder Diffraction, 28-ID-2) at the National Synchrotron Light Source II (NSLS-II), Brookhaven National Laboratory, USA. The photon wavelength is $0.185794\ \text{\AA}$. A large-area of amorphous-silicon-based detector was used to collect data to high values of momentum transfer ($Q_{\text{max}} = 24\ \text{\AA}^{-1}$). The raw images were integrated using software FIT2d [21]. Another code PDFgetX3 was used to correct the data for background contributions, Compton scattering and detector effects, and to Fourier transform the data to generate $G(r)$, the PDF $G(r) = 4\pi r [\rho(r) - \rho_0] = \frac{2}{\pi} \int_0^\infty Q [S(Q) - 1] \sin(Qr) dQ$, here $\rho(r)$ is the microscopic pair density, ρ_0 is the average number density and Q is magnitude of the scattering vector [22]. For elastic scattering $Q = 4\pi \sin(\theta)/\lambda$ with 2θ being the scattering angle and λ the wavelength of the radiation used. $S(Q)$ is the total scattering function.

2.5. First-principles calculations

Our first-principles density functional theory (DFT) calculations were performed using the Vienna Ab-initio Simulation Package (VASP) with projector augmented wave (PAW) potentials [23]. To deal with the exchange-correlation functional, generalized gradient approximation (GGA) of Perdew-Becke-Ernzerhof (PBE) was employed with spin polarization [24]. Meanwhile, optB86b-vdW functional was also used including a self-consistent van der Waals correction. We used two different sets of parameters: one for sampling lower energy configuration, the other for determining accurate total energy. For the sampling procedure, kinetic energy cutoff was 300 eV for the plane wave basis set and Γ -centered grids was approximately 4000 k-point per reciprocal atom. In order for accurate simulation, we expanded calculation ranges: plane-wave basis set cutoff energy of 520 eV and Γ -centered grids with density of 8000 k-points per reciprocal atom. We searched the intermediate phases during the Li-TiS_2 reaction using the Non-Equilibrium Phase Search (NEPS) method by exploring geometrically distinct Li/vacancy configurations on possible insertion sites of the TiS_2 structure Fig. S10 at different compositions (Li/vacancy ratios) [25–27]. The method was proceeded as follows: (i) Identify all possible intercalation sites in original structure of TiS_2 ($P\bar{3}m1$) using MINT [28]. (ii) Enumerate all distinctive symmetrical configurations with Enum for a series of compositions $\text{Li}_x\Box_{2-x}\text{TiS}_2$ ($0 < x < 4$, \Box : vacancy) [29]. (iii) Sample total energies of all the configurations. (iv) For the selected compositions, expected structures were ranked by their total energies; then, three structures having the lowest energy were chosen for further calculation with more strict parameters according to a reaction $\text{TiS}_2 + x\text{Li} \rightarrow \text{Li}_x\text{TiS}_2$. (v) Build a convex hull using the formation energies. Composition points on the hull were determined as intermediate phases. The averaged voltage (relative to Li/Li^+) corresponding to the lithiation reaction was then calculated using the negative of the reaction free energy per Li added following the convex hull ($T = 0\ \text{K}$) to form a series of constant voltage steps which can be seen as an approximation of the actual voltage profile [30]. At finite temperature (e.g. room temperature), all the voltage steps will be significantly rounded as a result of the entropic effects [31].

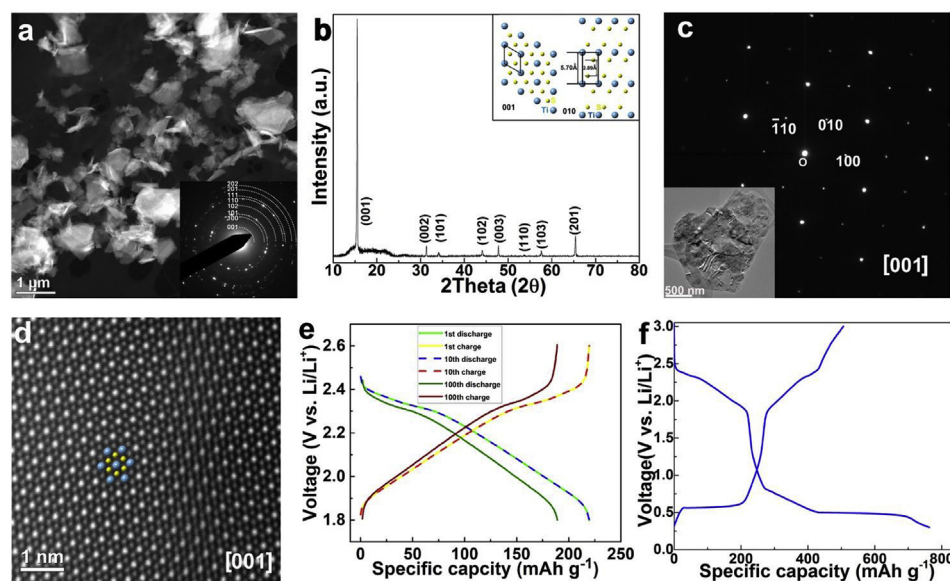


Fig. 1. Structure of pristine TiS_2 sample and its electrochemical performance. (a) STEM-ADF image, with corresponding SAED at inset. (b) XRD pattern with the inset showing the structure models of TiS_2 viewed along [001] and [010] zone axes. (c) Electron diffraction pattern and (inset) TEM-BF image of a single TiS_2 plate. (d) High-resolution HAADF-STEM image along [001] zone axis showing $P\bar{3}m1$ structure. (e) The charge/discharge profiles at 1st, 10th and 100th cycle at 0.1C discharged to 1.8 V. (f) Charge/discharge profiles of coin-cell batteries at 0.1C between 0.05 V and 2.6 V.

3. Results and discussion

3.1. The pristine TiS_2

Annular dark-field (ADF)-STEM image of the pristine TiS_2 samples used in this work is shown in Fig. 1a. The plate-like 1T- TiS_2 has a space group of $P\bar{3}m1$ ($a = 3.405 \text{ \AA}$, $c = 5.691 \text{ \AA}$ (PDF#15-0853)) confirmed by selected area electron diffraction (SAED) pattern (Fig. 1a, inset) and X-ray diffraction (XRD) pattern (Fig. 1b) [32]. The homogenous elemental distribution of Ti, S were confirmed by the STEM-electron energy-loss spectroscopy (EELS) mapping (Figs. S1a–c). The SAED pattern (Fig. 1c) and high-resolution high-angle annular dark-field (HAADF)-STEM image (Fig. 1d) acquired from a single TiS_2 flake show that the observing direction of nanoplates is along [001] zone axis [33]. Electrochemical properties of TiS_2 were tested in Li half-cell. When cycled between 1.8 V and 2.6 V at a rate of 0.1C, the 1st, 10th and 100th charge/discharge profiles are almost identical (Fig. 1e), which indicates an excellent reversibility of intercalation reaction. Fig. 1f shows the discharge-charge curves of the 1st cycle with cutoff voltages of 0.3 V (discharge) and 3 V (charge). Additional plateaus between 0.5 V and 0.8 V indicate other reactions beyond intercalation during further lithiation of layered LiTiS_2 . Cutting at 0.3 V, it shows a capacity of 763 mAh/g [34–36]. However, the voltage profiles and cyclic voltammetry (Figs. S2–S3) show that the reactions are only partially reversible during electrochemical cycles between 0.3 V and 3.0 V. The conversion reaction increases the capacity but also leads to structural degradation over cycling. It is possible to utilize the conversion reaction and regulate the intermediate phases and then prolonging cycling life [37].

3.2. In-situ TEM observation of expanded lithiation pathway of TiS_2

To identify the intermediate phases and define the reaction pathways [7,38–41], we employed a dry cell *in situ* TEM approach to study the structural evolutions over full lithiation range of TiS_2 [42–44]. The $\text{Li/Li}_2\text{O}$ on a tungsten tip directly touched the TiS_2 sample and a negative bias was applied to prompt the lithiation reaction [45]. Although there is no organic electrolyte involved in this experimental setup which limits its application on the formation of solid-electrolyte interphase, the lithiation inside the materials can be studied at a relative high resolution [43,45]. Fig. 2a and Fig. S4a show the radial intensity profiles of electron diffraction patterns as a function of reaction time derived from *in situ* SAED videos, which are presented at Movie S1, S2. The details of the data processing can be found at the supporting

information of Ref. [8]. It is obvious that the positions of the (h, k, l) (where $l \neq 0$) Bragg reflections are negatively shifted from 0 s to 122 s (Fig. 2a, yellow colored area) during lithiation, which corresponds to an increase of lattice parameters. Similar trend can be observed from the *in situ* SAED taken on a single flake of TiS_2 (Figs. S4–S5) while we observed a sudden change of lattice parameters in a single flake. By comparing the diffraction data with the reference profiles of TiS_2 (PDF#15-0853) and LiTiS_2 (PDF#28-0595) (Fig. S4a), the structural change can be attributed to a phase transition from TiS_2 ($P\bar{3}m1$) to layered LiTiS_2 ($P\bar{3}m1$). The lattice expansion during intercalation is expected as a sudden change, however, the intensity profiles in Fig. 2a show a gradual change due to the averaging effect from a large field of view. Although distortions at SAED patterns recorded by CCD camera can degrade the accuracy in determination of d -spacing, the error can be largely reduced by measuring the relative shift of diffraction spots/rings in *in situ* electron diffractions. Thus, the changes in d -spacing for (001), (101), (102) and (110) planes during the intercalation were precisely deduced as shown in Fig. S4b, 0.58% and 8.5% expansions along a and c directions, respectively. As a result of the intercalation reaction, the lithium ions occupy the octahedral sites between Ti-S slabs. While the Ti-S frame work has not been changed; however, the van der Waals interaction between Ti-S layers has been transferred to the covalent bonding between Li and S which holds neighboring chalcogenide layers firmly.

Supplementary data related to this article can be found at <https://doi.org/10.1016/j.nanoen.2019.103882>.

We found more lithium ions can be inserted into LiTiS_2 with further lithiation, found from 122 s to the end (600 s) and colored in blue as shown in Fig. 2a. The radial intensity profiles, variation of d -spacing, and selected diffraction patterns during the whole reaction process are shown in Fig. 2b–c and Fig. S6, respectively. *In situ* SAED reveals that the conversion reactions of TiS_2 undergo through two intermediate phases of Ti_2S (PDF#21-1286, $Pnmm$) and TiS (PDF#12-0534, $P6_3/mmc$), then finally end with a metallic Ti (PDF#51-0631, $P6/mmm$) phase as well as Li_2S . Ti_2S , TiS , and Ti were developed sequentially, and the formation of Li_2S (PDF#26-1188, $Fm\bar{3}m$) were noticed during the whole conversion processes. It is noteworthy that these phases were formed not from the direct conversion reactions proposed in Ref. [17], but from decomposition of LiTiS_2 . In addition, the final product of the conversion reaction is interestingly omega-Ti not the general structure of Ti such as alpha/beta-Ti [46,47]. This metallic phase exists under certain pressure and in our case, a high pressure could be induced by the large volume expansion (theoretically, 93.5% in volume) during

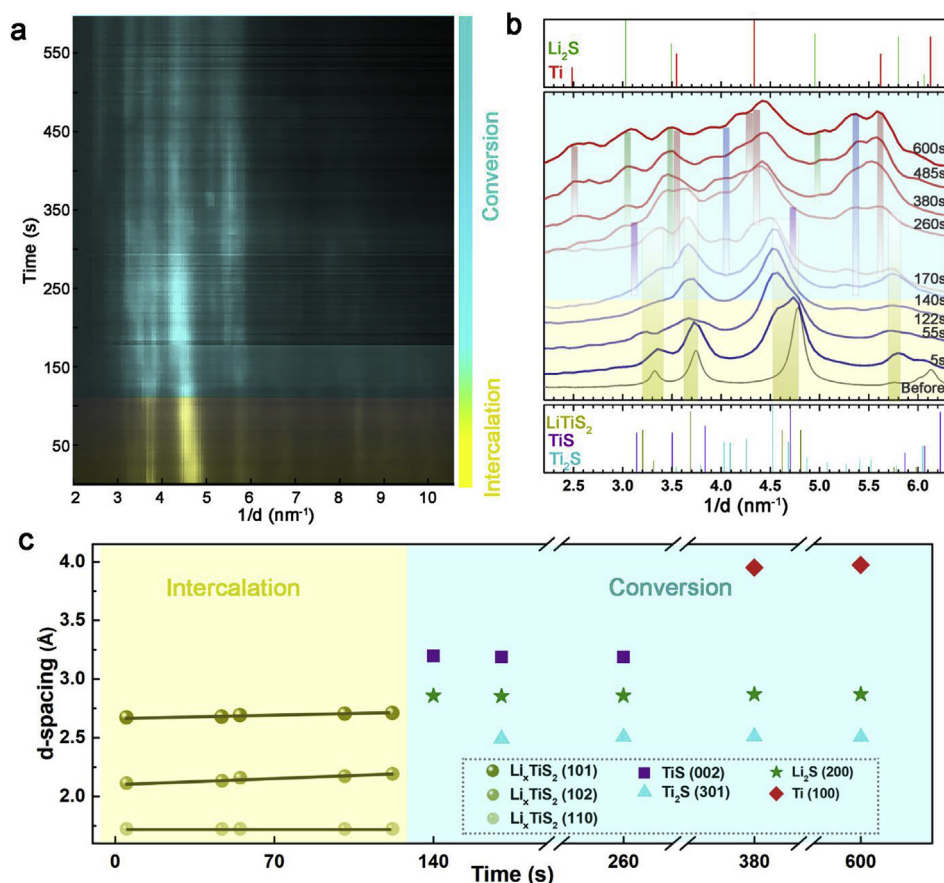


Fig. 2. Phase evolution during lithiation probed by *in situ* electron diffraction. (a) Electron diffraction intensity profile as a function of reaction time during an *in situ* lithiation of TiS_2 plates. (b) Radial intensity profiles of diffraction patterns at certain times. (c) Lattice constant changes measured from SAED during intercalation and conversion.

conversion reactions.

We investigated the intercalation process of TiS_2 in real space using *in situ* STEM imaging, as shown in Fig. 3 and Fig. S7. Time-series HAADF-STEM images in Fig. 3a, retrieved from Movie S3, show the intercalation process and the overlaid false colors indicate different phases: pristine TiS_2 in grey and Li_xTiS_2 in yellow. We chose HAADF-STEM images to monitor the changes during lithiation as contrast of HAADF-STEM image is sensitive to the averaged atomic number Z

[48,49]. The STEM images were recorded on a single nanosheet of TiS_2 close to $[001]$ zone axis. The intercalation reaction started from the touch point and propagated to the right. Schematic patterns of Fig. 3b illustrate the propagation of the reaction front with time. The whole intercalation process induces small volume change, which is consistent with *in situ* SAED patterns in Fig. 2. The projected areas of the emerged phases (Li_xTiS_2) and the corresponding propagation speed were measured as shown in Fig. 2c. The average reaction rate gradually increases

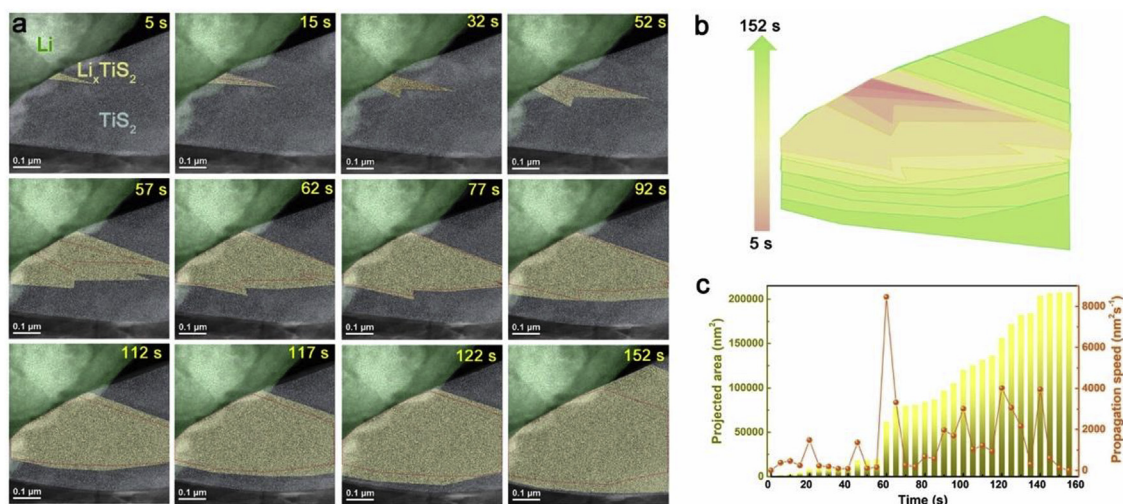


Fig. 3. *In situ* observation of phase transformation during lithiation. (a) HAADF-STEM image series showing phase evolution during lithiation. The overlaid false colors indicate different phases: pristine TiS_2 (grey) and Li_xTiS_2 (yellow) with dashed red lines illustrated margins of Li_xTiS_2 of previous states. (b) Schematic showing the propagation of Li_xTiS_2 with time. (c) Projected area of Li_xTiS_2 and propagation speed of intercalation as a function of time. (For interpretation of the references to color in this figure legend, the reader is referred to the Web version of this article.)

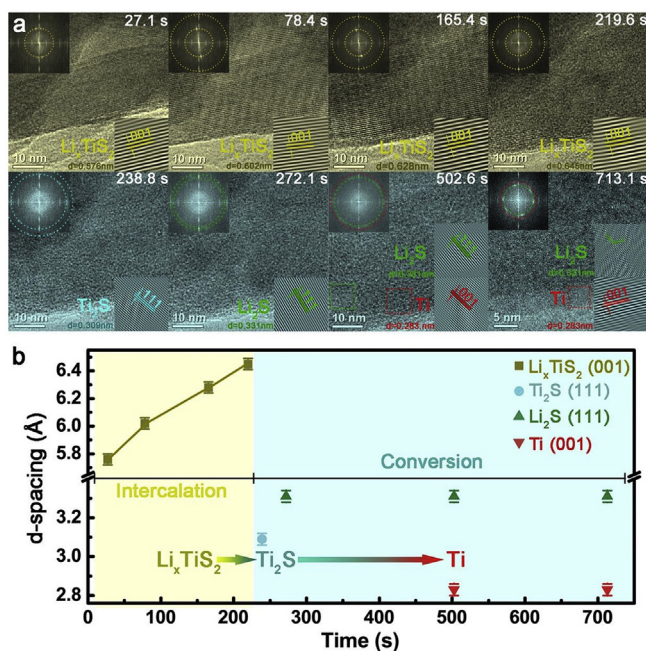


Fig. 4. Atomic resolution *in situ* TEM study. (a) HRTEM images in yellow indicating expansion of LiTiS_2 during *in situ* lithium intercalation and HRTEM images in green revealing existence of Ti_2S , Li_2S and Ti during *in situ* lithium conversion. Insets showing FFT patterns and enlarged filtered HRTEM images. (b) Lattice constants measured from Li_xTiS_2 (001), Ti_2S (111), Li_2S (111) and Ti (001) reflections indicating the intercalation and conversion reactions. (For interpretation of the references to color in this figure legend, the reader is referred to the Web version of this article.)

with time, which may result from that the inserted lithium ions expand the TiS_2 layers and make the following insertion of lithium ions easier. However, the reaction speed within one nanosheet is also affected by the local reaction environments such as overpotential, strain or the concentration of lithium ions and it is difficult to correlate this speed with the discharge rate in real battery test.

Supplementary data related to this article can be found at <https://doi.org/10.1016/j.nanoen.2019.103882>.

Considering that the large lattice expansion along c axis (8.5% from *in situ* SAED), we utilized an *in situ* HRTEM (Movie S4) to visualize the structural changes at high resolution. The time-sequence HRTEM images in Fig. 4a show the atomic structural evolution during lithiation. Corresponding fast Fourier transform (FFT) patterns and enlarged inverse FFT images are also shown as the insets of individual images confirming the existence of different phases during reaction. Two stages are assigned as intercalation and conversion reactions, respectively based on the changes in lattice parameters (Fig. 4b). HRTEM images in the top row of Fig. 4a clearly display the lattice expansion along c direction of TiS_2 during the lithium intercalation, which lasted from 0 s–219.6 s. However, we can observe a 12% change in the lattice parameters during the intercalation process which is larger than that from the *in situ* SAED. This is mainly due to the larger selected area of SAED ($\sim 1 \mu\text{m}$ by $1 \mu\text{m}$) where the diffraction information comes from all kinds of reacted areas as well as unreacted area, while the *in situ* HRTEM imaging only shows the local changes. Then the HRTEM images in blue reveal the emergence of Ti_2S , Li_2S and Ti phases during further lithium insertion as a result of conversion reactions. It is interesting that we did not see a completed decomposition of compounds observed in other conversion reactions but we observed the formation of Ti only at the edge of sample. These results are consistent with the *in situ* SAED analysis in Fig. 2. As chalcogenide materials are generally fragile under the electron beam, we performed controlled experiment to test beam

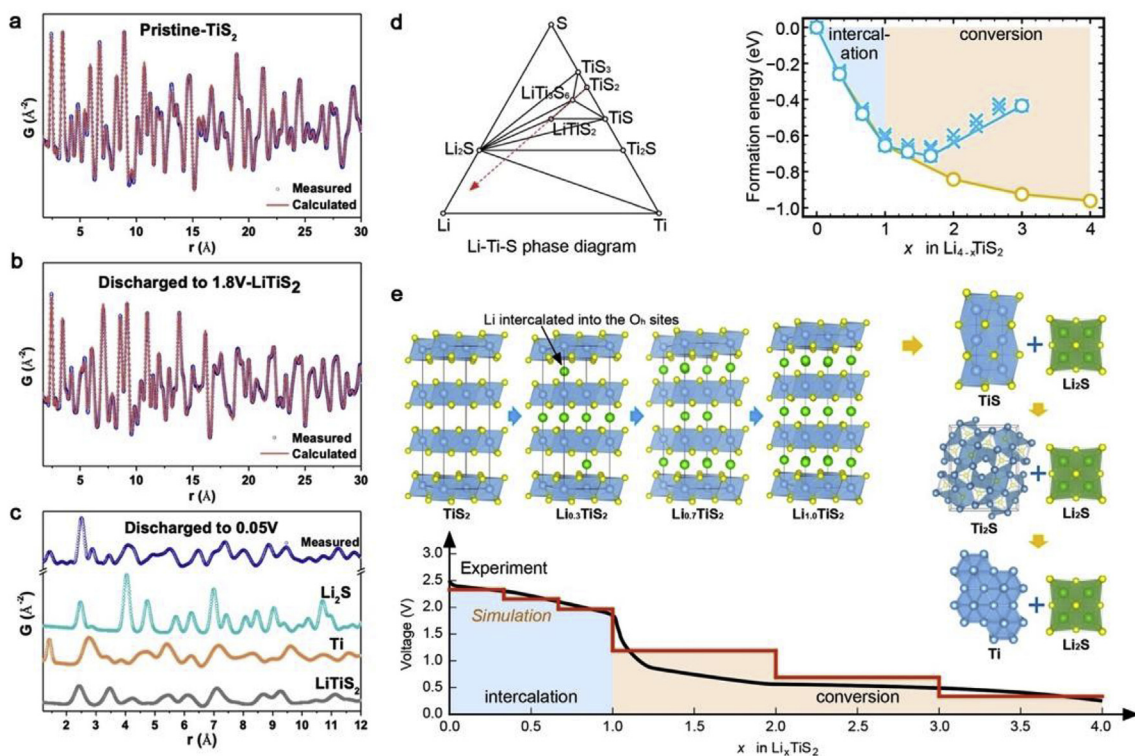


Fig. 5. Calibrated PDF results of TiS_2 samples at different states. (a) Pristine. (b) Discharged to 1.8 V. (c) Discharged to 0.05 V and reference files of Li_2S , Ti and LiTiS_2 . Theoretical calculation on the lithiation of TiS_2 . (d) Phase diagram from DFT calculation (left) and predicted two-step lithiation process based on the intermediate phase search (NEPS) method. (e) The voltage profile corresponding to the two-step lithiation process. Experimentally measured (black) and DFT calculated (red) discharge voltage profiles along with atomic models corresponding to the predicted intermediate phases during the intercalation ($0 < x < 1$) and conversion ($1 < x < 4$) processes of TiS_2 . (For interpretation of the references to color in this figure legend, the reader is referred to the Web version of this article.)

effect on TiS_2 sample. The *in situ* TEM imaging video and selected frames of controlled experiment (see experimental part for details) with corresponding FFT patterns are shown in Movie S5 and Fig. S8, which show no structural changes after an e-beam irradiation of 1400 s.

Supplementary data related to this article can be found at <https://doi.org/10.1016/j.nanoen.2019.103882>.

3.3. Ex-situ PDF and TEM characterization of lithiated TiS_2

The electrochemical reactions of electrodes in real cells may be different from that of *in situ* TEM dry cell. To clarify the possible discrepancy induced by experimental setups, ex-situ analysis of the TiS_2 electrode materials were also conducted with PDF, HRTEM, and STEM-EELS techniques. Fig. 5a–c shows the PDF results for TiS_2 at pristine, discharged to 1.8 V, and discharged to 0.05 V, respectively. The measured PDF profiles for the pristine and discharged to 1.8 V were well matched with calculated results of TiS_2 and LiTiS_2 , respectively. Whereas the PDF results for the sample discharged to 0.05 V could not be well fitted using references of Li_2S , $\omega\text{-Ti}$ and LiTiS_2 even though they have the features from these references. This is understandable because there should be the contributions from TiS and Ti_2S phases to the PDF pattern according to our *in situ* SAED results. The conversion reactions at coin cells were also investigated with the ex-situ STEM and STEM-EELS analysis at fully discharged state as shown in Fig. S9. Some cracks were observed in HAADF-STEM images, and inhomogeneous distributions of Ti, S and even O were observed with STEM-EELS elemental mapping, suggesting that the heterogeneous conversion reactions took place and induced strain to the flakes.

3.4. DFT calculations of the lithiation reaction of TiS_2

DFT calculations were performed to explore the lithiation of TiS_2 at equilibrium state. We constructed the Li–Ti–S ternary phase diagram at 0 K (Fig. 5d) by calculating the formation energies of all the known compounds of the Li–Ti–S chemical space from the Inorganic Crystal Structure Database (ICSD) [50–52]. The ground state reactions of Li– TiS_2 are found to proceed consequently through intercalation ($\text{TiS}_2 + 1/3\text{Li} \rightarrow \text{Li}_{1/3}\text{TiS}_2$; $\text{Li}_{1/3}\text{TiS}_2 + \text{Li} \rightarrow \text{LiTiS}_2$) and then conversion reactions ($\text{LiTiS}_2 + \text{Li} \rightarrow \text{TiS} + \text{Li}_2\text{S}$; $2\text{TiS} + 2\text{Li} \rightarrow \text{Ti}_2\text{S} + \text{Li}_2\text{S}$; $\text{Ti}_2\text{S} + 2\text{Li} \rightarrow 2\text{Ti} + \text{Li}_2\text{S}$). However, considering the possible existence of non-equilibrium phases as observed in previous works [2–4], we exploited our recently developed nonequilibrium phase search (NEPS) method [25–27], which identifies the possible non-equilibrium intermediate phases from a large number of geometrically distinct Li/vacancy configurations on possible insertion sites of the TiS_2 structure (Fig. S10) at different compositions (Li/vacancy ratios). Through calculating the formation energies of those configurations as shown in the built Li– TiS_2 convex hull (Fig. S10b), we find one extra non-equilibrium phase at $x = 0.7$ in Li_xTiS_2 , besides the identified ground state phases, which is consistent with previous reports [53,54]. With all the ground-state and non-equilibrium phases as discovered, now we have a full picture of the complete lithiation process of TiS_2 from the computational perspective. The pristine TiS_2 has two types of vacancies between Ti–S layers, namely octahedral and tetrahedral sites (Fig. S10a). Upon lithiation, the Li ions would start occupying the octahedral sites with subsequent formation of two intermediate phases ($x = 0.3$ and 0.7) until octahedral sites are completely filled up ($x = 1$). Further lithiation would have to be proceeded by taking the tetrahedral sites which are smaller in size compared to the octahedral counterparts. Ti–S bonds nearby will be greatly impacted and eventually be broken to lower the energy of the whole system (Fig. S10c). Beyond $x = 1$, the lithiation then proceeds via conversion reactions with lithiated products of $\text{TiS} + \text{Li}_2\text{S}$ ($x = 2$), $\text{Ti}_2\text{S} + \text{Li}_2\text{S}$ ($x = 3$), and finally $\text{Ti} + \text{Li}_2\text{S}$ ($x = 4$). We plotted the discharge voltage profile from the combined the NEPS and ground-state calculations, and overlaid with the experimental measurement (Fig. 5e), which shows a good agreement. Interestingly,

we observed only one intercalation process in both *in-situ* SAED and STEM-HAADF imaging, while the DFT calculation predicted three intercalation phases of $\text{Li}_{0.3}\text{TiS}_2$, $\text{Li}_{0.7}\text{TiS}_2$, and LiTiS_2 . One possibility is that the *in-situ* TEM technique could not detect the structural difference between these phases since there are only 0.25% in-plane lattice change from $\text{Li}_{0.3}\text{TiS}_2$ to $\text{Li}_{0.7}\text{TiS}_2$.

The reaction pathways of TiS_2 for the whole range of lithiation were investigated here with both theoretical calculations and real-time observations using TEM. Since there have been intensive studies on the intercalation process of TiS_2 , our work paid more attention to the conversion reactions. The insertion mechanisms can be varied depending on the metal cations [55,56]. For example, 2H-MoS_2 was firstly transformed to 1T-LiMoS_2 in a intercalation reaction and finally converted into the composite of metallic Mo and Li_2S upon lithiation [57,58]; whereas for the lithiation of copper sulfides (CuS or Cu_2S), a displacement reaction occurs after the intercalation: Cu is being extruded out of the original lattice, which is transformed into Li_2S [8,41]. A more complicated scenario was revealed during the lithiation of SnS_2 as four different types of reactions: intercalation, disordering, conversion, and alloying reactions happened sequentially [7,59]. In principle, configurations of Li–S/Ti–S bonds and kinetic factors play important roles to determine the reaction pathways. Comparing our results with the previous reports, we found that the reaction pathways of 2D metal sulfides were different for different M–S bonding. For example, the multiple-step conversion processes in TiS_2 in contrast to the single conversion step of SnS_2 though they have the same crystal structure. In addition, no alloying reaction has been found between metallic Ti and Li which might be due to the insolubility between Ti and Li metals. Although metallic Ti is a thermodynamically stable phase with further lithiation, after being discharged to 0.05 V, the Ti–S phases can be still observed from TEM images (Fig. S9). These intermediate phases may affect the performance of TiS_2 . In addition, the extrusion of Ti was observed at the edge of sample while the whole flakes are kept unbroken (Fig. 2). A recent report has shown that extrusion reaction with relative intact matrix can enhance the cycling stability and reaction kinetics compared to the conversion [60]. While the conversion reactions are severely irreversible in most other metal sulfides, the cyclic charge/discharge curves of TiS_2 (Fig. S2) show a retention of more than 50% of capacity after 9 cycles in spite of fast decay, indicating the conversion reactions are partially reversible [7]. We believe that the intermediate phases of Ti–S and extrusion reaction can be beneficial to the reversibility of TiS_2 because the relative intact structure of Ti–S phase can serve as the diffusion paths for lithium ions and electrons, reducing passivation layers produced from conversion reaction. The partial reversibility we found in TiS_2 indicates that TiS_2 can be developed as a promising electrode material for lithium ion batteries.

4. Conclusions

In summary, we take advantage of a correlated study of *in situ* TEM characterization and DFT calculations to elucidate atomistic lithiation mechanisms of 2D metallic sulfide compound. As DFT calculations predict the possibility of expanded lithiation in TiS_2 beyond intercalation, we reveal the reaction pathways experimentally using *in situ* TEM methods. The intercalation of Li into TiS_2 proceeds along and opens the gap between TiS_2 slabs. LiTiS_2 phase formed after the intercalation reaction. The *in situ* electron diffraction shows a high accuracy measurement of the lattice modifications and reveals a multi-step conversion reaction with further lithiation of LiTiS_2 . Two intermediate phases of TiS and Ti_2S are found along with the formation of Li_2S . Finally, a metallic Ti phase is identified from both *in situ* TEM and ex-situ characterizations of TEM and PDF. This result shows up to 4 lithium ions can be inserted into one chemical formula of TiS_2 , which largely increase the capacity. With lithium metal as anode, this expanded capacity can double the total energy density of Li– TiS_2 battery. More importantly, the multiple step reactions may account for the improved

reaction reversibility and make TiS_2 a promising candidate for electrode materials for lithium ion batteries. A first-principles calculation guided *in situ* TEM approach here sheds light on revealing new reaction mechanisms of electrode materials and show the metal-sulfur bond of 2D metal sulfides plays a determining role for their reaction pathways.

Acknowledgements

Electron microscopy work was performed at the Center for Functional Nanomaterials, Brookhaven National Laboratory, which is supported by the U.S. Department of Energy, Office of Basic Energy Science, under contract No. DE-SC0012704. M.Fu acknowledge the support of Visiting Scholar Research Program of NPU, the Fundamental Research Funds for the Central Universities (31020195C001) and Innovation and Development Program of Shaanxi Province (2017KTPT-03). Z.Y. (DFT calculations, analysis of results) and C.W. (leadership of DFT calculations) were supported as part of the Center for Electrochemical Energy Science (CEES), an Energy Frontier Research Center funded by the U.S. Department of Energy, Office of Science, Basic Energy Sciences under Award No. DE-AC02-06CH11357. The authors gratefully acknowledge the computing resources from the National Energy Research Scientific Computing Center, a DOE Office of Science User Facility supported by the Office of Science of the U.S. Department of Energy under Contract No. DE-AC02-05CH11231. This research used 28-ID-2 (XPD) of the National Synchrotron Light Source II, a U.S. Department of Energy Office of Science User Facility operated for the DOE Office of Science by Brookhaven National Laboratory under Contract No. DE-SC0012704. H.D. and Y.Y. acknowledges funding support from the U.S. Department of Energy's Office of Energy Efficiency and Renewable Energy (DE-EE0008234), UH Technical Gap Fund, and UH High Priority Area Large Equipment Grant.

Appendix A. Supplementary data

Supplementary data to this article can be found online at <https://doi.org/10.1016/j.nanoen.2019.103882>.

References

- M. Armand, J.-M. Tarascon, Building better batteries, *Nature* 451 (2008) 652–657.
- H. Liu, F.C. Strobridge, O.J. Borkiewicz, K.M. Wiaderek, K.W. Chapman, P.J. Chupas, C.P. Grey, Capturing metastable structures during high-rate cycling of LiFePO_4 nanoparticle electrodes, *Science* 344 (2014) 1252817–1252817.
- H. Liu, Q. Li, Z. Yao, L. Li, Y. Li, C. Wolverton, M.C. Hersam, V.P. Dravid, Origin of fracture-resistance to large volume change in Cu-substituted Co_3O_4 electrodes, *Adv. Mater.* 30 (2017) 1704851–1704858.
- Q. Li, J. Wu, Z. Yao, M.M. Thackeray, C. Wolverton, V.P. Dravid, Dynamic imaging of metastable reaction pathways in lithiated metal oxide electrodes, *Nano Energy* 44 (2017) 15–22.
- E. Hu, X. Yu, R. Lin, X. Bi, J. Lu, S. Bak, K.W. Nam, H.L. Xin, C. Jaye, D.A. Fischer, K. Amine, X.Q. Yang, Evolution of redox couples in Li- and Mn-rich cathode materials and mitigation of voltage fade by reducing oxygen release, *Nat. Energy* 3 (2018) 690–698.
- A. Singer, A. Ulvestad, H.-M. Cho, J.W. Kim, J. Maser, R. Harder, Y.S. Meng, O.G. Shpyrko, Nonequilibrium structural dynamics of nanoparticles in $\text{LiNi}_{1/2}\text{Mn}_{3/2}\text{O}_4$ cathode under operando conditions, *Nano Lett.* 14 (2014) 5295–5300.
- S. Hwang, Z. Yao, L. Zhang, M. Fu, K. He, L. Mai, C. Wolverton, D. Su, Multistep lithiation of tin sulfide: an investigation using *in situ* electron microscopy, *ACS Nano* 12 (2018) 3638–3645.
- K. He, Z. Yao, S. Hwang, N. Li, K. Sun, H. Gan, Y. Du, H. Zhang, C. Wolverton, D. Su, Kinetically-driven phase transformation during lithiation in copper sulfide nanoflakes, *Nano Lett.* 17 (2017) 5726–5733.
- Y. Yuan, K. Amine, J. Lu, R. Shahbazian-Yassar, Understanding materials challenges for rechargeable ion batteries with *in situ* transmission electron microscopy, *Nat. Commun.* 8 (2017) 15806.
- J. Li, G. Johnson, S. Zhang, D. Su, *In situ* transmission electron microscopy for energy applications, *Joule* 3 (2019) 4–8.
- W. Li, B. Song, A. Manthiram, High-voltage positive electrode materials for lithium-ion batteries, *Chem. Soc. Rev.* 46 (2017) 3006–3059.
- C. Zhu, R.E. Usiskin, Y. Yu, J. Maier, The nanoscale circuitry of battery electrodes, *Science* 358 (2017).
- X. Huang, Z. Zeng, H. Zhang, Metal dichalcogenide nanosheets: preparation, properties and applications, *Chem. Soc. Rev.* 42 (2013) 1934–1946.
- E.J. Frazer, S. Phang, Titanium disulphide as a cathode material in lithium batteries - a review, *J. Power Sources* 6 (1981) 307–317.
- M.S. Whittingham, Electrical energy storage and intercalation chemistry, *Science* 192 (1976) 1126–1127.
- M.S. Whittingham, The hydrated intercalation complexes of the layered disulfides, *Mater. Res. Bull.* 9 (1974) 1681–1689.
- M.S. Whittingham, The role of ternary phases in cathode reactions, *J. Electrochem. Soc.* 123 (1976) 315.
- T.A. Yersak, J.E. Trevey, S.H. Lee, *In situ* lithiation of TiS_2 enabled by spontaneous decomposition of Li_3N , *J. Power Sources* 196 (2011) 9830–9834.
- R.F. Egerton, P. Li, M. Malac, Radiation damage in the TEM and SEM, *Micron* 35 (2004) 399–409.
- D. Su, F. Wang, C. Ma, N. Jiang, Engineering nano-composite $\text{Li}_4\text{Ti}_5\text{O}_{12}$ anodes via scanning electron-probe fabrication, *Nano Energy* 2 (2013) 343–350.
- A.P. Hammersley, S.O. Svensson, M. Hanfland, A.N. Fitch, D. Hausermann, Two-dimensional detector software: from real detector to idealised image or two-theta scan, *High Press. Res.* 14 (1996) 235–248.
- P. Juhás, T. Davis, C.L. Farrow, S.J.L. Billinge, PDFgetX3: a rapid and highly automatable program for processing powder diffraction data into total scattering pair distribution functions, *J. Appl. Crystallogr.* 46 (2013) 560–566.
- G. Kresse, J. Hafner, *Ab initio* molecular dynamics for liquid metals, *Phys. Rev. B* 47 (1993) 558–561.
- P.E. Blöchl, Projector augmented-wave method, *Phys. Rev. B* 50 (1994) 17953–17979.
- Z. Yao, S. Kim, M. Aykol, Q. Li, J. Wu, J. He, C. Wolverton, Revealing the conversion mechanism of transition metal oxide electrodes during lithiation from first-principles, *Chem. Mater.* 29 (2017) 9011–9022.
- Z. Yao, S. Kim, J. He, V.I. Hegde, C. Wolverton, Interplay of cation and anion redox in $\text{Li}_4\text{Mn}_2\text{O}_5$ cathode material and prediction of improved $\text{Li}_4(\text{Mn},\text{M}_2)\text{O}_5$ electrodes for Li-ion batteries, *Sci. Adv.* 4 (2018) 6754.
- C. Zhan, Z. Yao, J. Lu, L. Ma, V.A. Maroni, L. Li, E. Lee, E.E. Alp, T. Wu, J. Wen, Y. Ren, C. Johnson, M.M. Thackeray, M.K.Y. Chan, C. Wolverton, K. Amine, Enabling the high capacity of lithium-rich anti-fluorite lithium iron oxide by simultaneous anionic and cationic redox, *Nat. Energy* 2 (2017) 963–971.
- L. Ward, K. Michel, *Materials/Mint*, Initial Release, 2016.
- G.L.W. Hart, R.W. Forcade, Algorithm for generating derivative structures, *Phys. Rev. B* 77 (2008) 224115.
- M.K.Y. Chan, C. Wolverton, J.P. Greeley, First principles simulations of the electrochemical lithiation and delithiation of faceted crystalline silicon, *J. Am. Chem. Soc.* 134 (2012) 14362–14374.
- C. Wolverton, A. Zunger, First-principles prediction of vacancy order-disorder and intercalation battery voltages in Li_2CoO_2 , *Phys. Rev. Lett.* 81 (1998) 606–609.
- H.D. Yoo, Y. Liang, H. Dong, J. Lin, H. Wang, Y. Liu, L. Ma, T. Wu, Y. Li, Q. Ru, Y. Jing, Q. An, W. Zhou, J. Guo, J. Lu, S.T. Pantelides, X. Qian, Y. Yao, Fast kinetics of magnesium monochloride cations in interlayer-expanded titanium disulfide for magnesium rechargeable batteries, *Nat. Commun.* 8 (2017) 1–10.
- Y. Yu, G.-H. Nam, Q. He, X.-J. Wu, K. Zhang, Z. Yang, J. Chen, Q. Ma, M. Zhao, Z. Liu, F.-R. Ran, X. Wang, H. Li, X. Huang, B. Li, Q. Xiong, Q. Zhang, Z. Liu, L. Gu, Y. Du, W. Huang, H. Zhang, High phase-purity $1\text{T}'\text{-MoS}_2$ - and $1\text{T}'\text{-MoSe}_2$ -layered crystals, *Nat. Chem.* 10 (2018) 638–643.
- X. Bian, Y. Gao, Q. Fu, S. Indris, Y. Ju, Y. Meng, F. Du, N. Bramnik, H. Ehrenberg, Y. Wei, A long cycle-life and high safety $\text{Na}^+/\text{Mg}^{2+}$ hybrid-ion battery built by using a TiS_2 derived titanium sulfide cathode, *J. Mater. Chem. A* 5 (2017) 600–608.
- X. Sun, P. Bonnick, L.F. Nazar, Layered TiS_2 positive electrode for Mg batteries, *ACS Energy Lett* 1 (2016) 297–301.
- B. Tian, W. Tang, K. Leng, Z. Chen, S.J.R. Tan, C. Peng, G.-H. Ning, W. Fu, C. Su, G.W. Zheng, K.P. Loh, Phase transformations in TiS_2 during K intercalation, *ACS Energy Lett* 2 (2017) 1835–1840.
- Y. Yuan, A. Nie, G.M. Odegard, R. Xu, D. Zhou, S. Santhanagopalan, K. He, H. Asayesh-Ardakani, D.D. Meng, R.F. Klie, C. Johnson, J. Lu, R. Shahbazian-Yassar, Asynchronous crystal cell expansion during lithiation of K^+ -stabilized $\alpha\text{-MnO}_2$, *Nano Lett.* 15 (2015) 2998–3007.
- J. Feng, K. Liu, M. Graf, M. Lihter, R.D. Bulushev, D. Dumcenco, D.T.L. Alexander, D. Krasnozhan, T. Vuletic, A. Kis, A. Radenovic, Electrochemical reaction in single layer MoS_2 : nanopores opened atom by atom, *Nano Lett.* 15 (2015) 3431–3438.
- M. Azhagurajan, T. Kajita, T. Itoh, Y.-G. Kim, K. Itaya, *In situ* visualization of lithium ion intercalation into MoS_2 single crystals using differential optical microscopy with atomic layer resolution, *J. Am. Chem. Soc.* 138 (2016) 3355–3361.
- P. Gao, Y.-Y. Zhang, L. Wang, S. Chen, Y. Huang, X. Ma, K. Liu, D. Yu, *In situ* atomic-scale observation of reversible sodium ions migration in layered metal dichalcogenide SnS_2 nanostructures, *Nano Energy* 32 (2017) 302–309.
- M.T. McDowell, Z. Lu, K.J. Koski, J.H. Yu, G. Zheng, Y. Cui, *In situ* observation of divergent phase transformations in individual sulfide nanocrystals, *Nano Lett.* 15 (2015) 1264–1271.
- T. Shang, Y. Wen, D. Xiao, L. Gu, Y. Hu, H. Li, Atomic-scale monitoring of electrode materials in lithium-ion batteries using *in situ* transmission electron microscopy, *Adv. Energy Mater.* 7 (2017) 1700709.
- K. He, Y. Zhou, P. Gao, L. Wang, N. Pereira, G.G. Amatucci, K.W. Nam, X.Q. Yang, Y. Zhu, F. Wang, D. Su, Sodiation via heterogeneous disproportionation in FeF_2 electrodes for sodium-ion batteries, *ACS Nano* 8 (2014) 7251–7259.
- Y. Liu, N.S. Hudak, D.L. Huber, S.J. Limmer, J.P. Sullivan, J.Y. Huang, *In situ* transmission electron microscopy observation of pulverization of aluminum nanowires and evolution of the thin surface Al_2O_3 layers during lithiation and delithiation cycles, *Nano* 11 (2011) 4188–4194.
- J.Y. Huang, L. Zhong, C.M. Wang, J.P. Sullivan, W. Xu, L.Q. Zhang, S.X. Mao, N.S. Hudak, X.H. Liu, A. Subramanian, H. Fan, L. Qi, A. Kushima, J. Li, *In situ* observation of the electrochemical lithiation of a single SnO_2 nanowire electrode,

- Science 330 (2010) 1515–1520.
- [46] Y. Vohra, P. Spencer, Novel γ -phase of titanium metal at megabar pressures, *Phys. Rev. Lett.* 86 (2001) 3068–3071.
- [47] S.K. Sikka, Y.K. Vohra, R. Chidambaram, Omega phase in materials, *Prog. Mater. Sci.* 27 (1982) 245–310.
- [48] A. Ohtomo, D.A. Muller, J.L. Grazul, H.Y. Hwang, Artificial charge-modulation in atomic-scale perovskite titanate superlattices, *Nature* 419 (2002) 378–380.
- [49] J. Li, K. He, Q. Meng, X. Li, Y. Zhu, S. Hwang, K. Sun, H. Gan, Y. Zhu, Y. Mo, E.A. Stach, D. Su, Kinetic phase evolution of spinel cobalt oxide during lithiation, *ACS Nano* 10 (2016) 9577–9585.
- [50] A. Belsky, M. Hellenbrandt, V.L. Karen, P. Luksch, New developments in the Inorganic Crystal Structure Database (ICSD): accessibility in support of materials research and design, *Acta Crystallogr. Sect. B Struct. Sci.* 58 (2002) 364–369.
- [51] S. Kirklín, J.E. Saal, B. Meredig, A. Thompson, J.W. Doak, M. Aykol, S. Rühl, C. Wolverton, The Open Quantum Materials Database (OQMD): assessing the accuracy of DFT formation energies, *Npj Comput. Mater.* 1 (2015) 15010.
- [52] J.E. Saal, S. Kirklín, M. Aykol, B. Meredig, C. Wolverton, Materials design and discovery with high-throughput density functional theory: the open quantum materials database (OQMD), *JOM (J. Occup. Med.)* 65 (2013) 1501–1509.
- [53] H.A. Hallak, P.A. Lee, Lithium ordering in Li_xTiS_2 : a superlattice structure for $\text{Li}_{0.33}\text{TiS}_2$, *Solid State Commun.* 47 (1983) 503–505.
- [54] D. Wiedemann, S. Nakhai, A. Senyshyn, T. Bredow, M. Lerch, The high-temperature transformation from 1T^- to $3\text{r-Li}_x\text{TiS}_2$ ($x = 0.7, 0.9$) as observed in situ with neutron powder diffraction, *Zeitschrift Fur Phys. Chemie.* 229 (2015) 1275–1288.
- [55] Q. Li, Y. Xu, Z. Yao, J. Kang, X. Liu, C. Wolverton, M.C. Hersam, J. Wu, V.P. Dravid, Revealing the effects of electrode crystallographic orientation on battery electrochemistry via the anisotropic lithiation and sodiation of ReS_2 , *ACS Nano* (2018) 1–20.
- [56] H. Liu, Q. Li, Z. Yao, L. Li, Y. Li, C. Wolverton, M.C. Hersam, J. Wu, V.P. Dravid, Origin of fracture-resistance to large volume change in Cu-substituted Co_3O_4 electrodes, *Adv. Mater.* 30 (2018) 1704851.
- [57] Q. Su, S. Wang, M. Feng, G. Du, B. Xu, Direct studies on the lithium-storage mechanism of molybdenum disulfide, *Sci. Rep.* 7 (2017) 7275.
- [58] Y. Cheng, A. Nie, Q. Zhang, L.-Y. Gan, R. Shahbazian-Yassar, U. Schwingenschlogl, Origin of the phase transition in lithiated molybdenum disulfide, *ACS Nano* 8 (2014) 11447–11453.
- [59] P. Gao, L. Wang, Y.Y. Zhang, Y. Huang, L. Liao, P. Sutter, K. Liu, D. Yu, E.G. Wang, High-resolution tracking asymmetric lithium insertion and extraction and local structure ordering in SnS_2 , *Nano Lett.* 16 (2016) 5582–5588.
- [60] X. Fan, E. Hu, X. Ji, Y. Zhu, F. Han, S. Hwang, J. Liu, S. Bak, Z. Ma, T. Gao, S.C. Liou, J. Bai, X.Q. Yang, Y. Mo, K. Xu, D. Su, C. Wang, High energy-density and reversibility of iron fluoride cathode enabled via an intercalation-extrusion reaction, *Nat. Commun.* 9 (2018) 1–12.